Growth, morphology, and optical and electrical properties of semicontinuous metallic films

Katyayani Seal, Mark A. Nelson,* and Z. Charles Ying
Department of Physics, New Mexico State University, Las Cruces, New Mexico 88003-8001

Dentcho A. Genov, Andrey K. Sarychev, and Vladimir M. Shalaev
School of Electrical and Computer Engineering, Purdue University, West Lafayette, Indiana 47907-1285

(Received 19 June 2002; revised manuscript received 9 October 2002; published 22 January 2003)

The growth and optical properties of semicontinuous silver films on insulator substrates were studied experimentally and theoretically. In the experimental studies, films were synthesized by the pulsed-laser deposition technique, characterized by electron microscopy and *in situ* optical and dc electrical resistance measurements and studied using near-field optical microscopy. The percolation threshold of the films was found to be at ~65% metal filling fraction, higher than the 50%–60% range of values predicted for two-dimensional (2D) bond or site percolation films and suggesting the importance of grain coalescence and 3D growth in our system. Local optical properties measured by near-field optical microscopy were compared with theoretical results obtained using the block-elimination method, with good agreement. Local-field distributions were found to depend strongly on the metal concentration and wavelength of illumination. The degree of localization was found to increase at metal concentrations both above and below the percolation threshold. At a very high metal coverage, very strong local fields were observed in submicron voids of a metal dielectric film. These fields are likely due to localized surface plasmon polaritons.

DOI: 10.1103/PhysRevB.67.035318 PACS number(s): 78.20.−e, 73.20.Mf, 07.79.Fc

I. INTRODUCTION

Random metal-dielectric composites, such as nanoscaled semicontinuous metallic structures, exhibit optical and electrical transport properties that are notably different from those of their corresponding bulk counterparts.[1–20] One of the most remarkable properties of such composite systems is the localization and enhancement of electric and magnetic fields in the visible and infrared spectral ranges.[6–8] These materials show promise in applications such as single molecular spectroscopy,[21] broadband optical amplifiers, and optical limiters.[22]

The synthesis of metal-dielectric composites typically involves the deposition of metal particles onto a dielectric substrate.[23,24] At low metal concentrations, mutually separated nanometer-sized grains are formed on the substrate. Self-similar clusters form as the metal concentration (filling fraction) increases. The geometrical properties of these nanostructures, e.g., the scale invariance or fractality of the clusters, play an important role in determining the physical properties of these systems.[1–3,6–8,25] At a metal concentration called the percolation threshold (p_c) initially separated clusters interconnect to form an infinite cluster of metal, enabling a continuous current path in the system. The percolation threshold marks an insulator-to-metal phase transition and is accompanied by a sharp drop in dc resistivity[9] and anomalous absorption at visible and near-infrared wavelengths.[1,4,26,27] At even higher metal concentrations, the sample becomes mostly metallic with dielectric voids, ultimately resulting in a uniform metal film.

The unique geometrical properties of semicontinuous metallic films near the percolation threshold lead to localization of surface plasmons, an effect related to Anderson localization.[1,8] As a result, electromagnetic energy is also concentrated in nanometer-sized areas (called hot spots) where electric and magnetic fields are strongly enhanced in comparison to the incident field. These localized electromagnetic field fluctuations in metal-dielectric systems are especially prominent at optical and near-infrared wavelengths where the resulting local fields can exceed the incident field by up to 10^5 for the linear and up to 10^{20} for the nonlinear optical responses, such as four-wave mixing.[1–3] This phenomenon was predicted by a scaling theory[1,6,8] and verified by numerical calculations and computer simulations that use real-space renormalization group procedures[1,7,8] and block elimination[10] as well. The spatial locations of the field maxima depend on the polarization, wavelength, and angle of incidence of the applied field.[16] The distribution (both separation and magnitude) of the local field is also expected to vary with metal concentration, a phenomenon that has not been experimentally investigated in the past.

The theoretical treatment of high-order local-field enhancement in percolation systems was established just recently.[4–8] Theory shows that, for the special case of surface plasmon resonance in individual metal particles at $\varepsilon_d = -\mathrm{Re}(\varepsilon_m)$ (where ε_d and ε_m are the dielectric functions of the dielectric and metallic components, respectively), the problem of the field potential distribution across the sample can be mapped to the Anderson transition problem. The localization and optical properties at the limit $|\varepsilon_m/\varepsilon_d| \gg 1$, which is valid for the samples studied in this paper, can be found by the scale-renormalization method developed by Sarychev and Shalaev.[4–8] The predicted localization phenomenon has been verified experimentally[11,16] and theoretically by using an approximate numerical scheme[7] and later by using an exact block-elimination procedure.[10] It was found that in the vicinity of the percolation threshold p_c, the local field has a very wide log-normal distribution which transforms into a power-law distribution away from p_c. Similar power-law distributions were found theoretically for fractal aggregates[12]

 ©2003 The American Physical Society

where, as in the case of the metal-dielectric composites, the exponent was close to the "single-dipole" value of 1.5. Experimental studies of the intensity distribution in nanostructured surfaces were performed in Ref. 17. However, until now the intensity distributions in metal-dielectric films at the percolation threshold have never been studied.

This paper reports a systematic experimental analysis of the changes in the local optical properties, morphology, and electrical conductivity with metal concentration and corroborates it with theoretical models. The films are grown using laser ablation and characterized by transmission electron microscopy, scanning electron microscopy, *in situ* resistance measurements, and *in situ* optical measurements, in addition to a near-field scanning optical microscopy (NSOM) investigation at two incident wavelengths (543 and 633 nm).

The theoretical calculations for the local optical response are based on an exact numerical method: the block elimination method. The local field is distributed randomly over the sample surface, and the intensity distributions and enhancement magnitudes in NSOM images are dependent on the microscope resolution and other characteristics of the NSOM configuration.[28] It is therefore useful to employ statistical treatments of these images as consistent method of analyzing the sample properties. The probability distribution function (PDF) for the local-field intensities provides a quantitative estimate of the intensity changes over the sample area.[17] The theoretical local-field calculations have been averaged to account for the resolution limit of the NSOM used so that theory and experiment can be more effectively compared via the PDF, which was found to transform from a wide log-normal dependence to a power-law dependence when the averaging procedure was carried out.

The rest of this paper is organized as follows: in Sec. II details of the experiment are described, while Sec. III briefly covers the theoretical calculations and averaging methods used in our studies. In Sec. IV both the experimental and theoretical results are presented and discussed. Conclusions are provided in Sec. V.

II. EXPERIMENTAL PROCEDURE

The random metal-dielectric films used in our experimental study were synthesized by laser ablation of a solid silver target under argon gas pressure of 0.3 mTorr (0.04 Pa). A nanosecond Nd:YAG laser (Quanta-Ray DCR-02A) provided pulses with an energy of 100 mJ/pulse, a repetition rate of 10 Hz, and a wavelength of 532 nm. The spot size of the laser beam at the target was approximately 1 mm^2. Glass substrates for NSOM study, Formvar-coated copper grids for characterization by transmission electron microscopy (TEM), and silicon substrates for scanning electron microscopy (SEM) analysis were placed horizontally at a predetermined distance from the target.

Silver was the metal of choice for these experiments because it exhibits strong resonances at frequencies in the visible range. Also, its dielectric constant has a large negative real part and a relatively small imaginary part compared to transition metals so that optical enhancement is expected to be large. Similar behavior is expected for gold and other coinage metals.

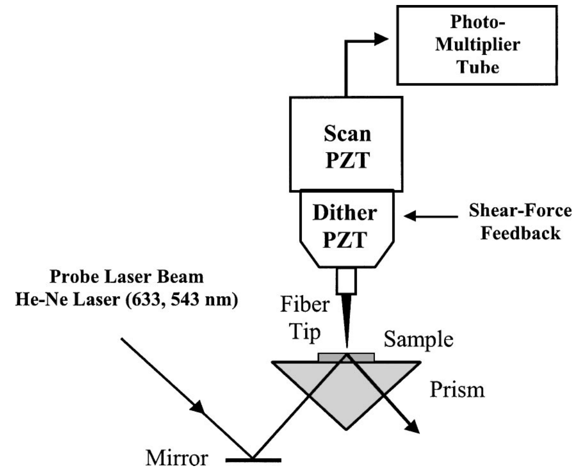

FIG. 1. Schematic of experimental NSOM apparatus.

The films were characterized *in situ* by their electrical resistance using an electrometer (Keithley 610C) and by their optical transmittance and reflectance. In the optical measurements, a diode laser (Melles Griot 06-DAL-103) operating at 650 nm provided the incident beam and power meters (Newport 1830C) were used to measure the power of the transmitted and reflected beams. The absorption profile was computed from the transmittance and reflectance data, and this helped to mark the percolation threshold concentration.

Electron microscopy was used to study the microstructure of the samples. A TEM (Hitachi H-7000) was used to study the silver films deposited on Formvar-coated copper grids, a type of standard TEM substrate. The glass substrate used for NSOM is not suitable for electron microscopy measurements because of its large thickness and low electrical conductivity. In order to investigate possible differences in the morphologies of the silver films deposited on glass and Formvar, additional studies were carried out using a SEM with a field-emission gun (Hitachi S-800) for samples of silver films deposited on substrates of semiconductor silicon and Formvar-coated copper grids. The surface of silicon has a native SiO_2 layer, which serves as a good representation of the SiO_2 glass substrate used for NSOM. The SEM results indicate qualitatively similar morphologies for the silver films deposited on SiO_2 and Formvar (for details, see Sec. IV A).

The silver-glass samples with different metal concentrations were analyzed by a NSOM (Quesant Q250), which was modified from a commercial atomic force microscope (AFM). Samples were mounted on the hypotenuse face of a BK7 glass prism with index matching fluid and illuminated by the evanescent field in the total internal-reflection geometry as shown in Fig. 1. The angle of the incident beam was $\theta = 47°$. The illumination sources were helium-neon lasers operating at wavelengths of 543 and 633 nm. The local optical signal was collected by a tapered, uncoated optical fiber with a tip radius of about 50 nm and fed to a photomultiplier tube. A fiber puller (Sutter Instruments P-2000) was used to

taper the optical fiber. Tip-sample separation during the NSOM experiments was maintained at a distance of $h \sim 10$ nm during NSOM experiments by using nonoptical shear-force feedback.[29] All NSOM data presented in this paper were normalized with respect to the intensity of the evanescent field, which was obtained by measuring the average intensity value for a clear glass substrate. It was ensured that the evanescent field, when measured at a height h above the sample surface (tip-sample separation is h), does not decay significantly as compared to the evanescent field at the sample surface ($h=0$) by using the formula

$$I_{\text{measured}}=I_0 \exp\left(-\frac{2\pi h\sqrt{(n\sin\theta)^2-1}}{\lambda}\right), \tag{1}$$

where λ is the light wavelength in vacuum and $n \approx 1.5$ is the index of refraction of the glass substrate. At a height of $h=10$ nm, the signal loss is only 4.5%.

III. THEORY AND NUMERICAL CALCULATIONS

In the limit of small particle sizes $a \ll \lambda$, where λ is the wavelength of the incident beam, one can introduce a local potential $\phi(\mathbf{r})$ to describe the local electric field properties of metal-dielectric films.[4] In the quasistatic approximation we have the current conservation law $\nabla \cdot [\sigma(\mathbf{r})(-\nabla\phi(\mathbf{r})+E_0)]=0$, where E_0 is the incident electric field. The spatially dependent conductivity $\sigma(\mathbf{r})$ alternately takes the value σ_d for the dielectric voids and σ_m for the metal particles. To solve the current conservation law we discretize the differential equation over a square lattice of size L, where each site is connected to the neighboring sites through four bonds. Each bond in the square lattice takes a value for conductivity, σ_m or σ_d, with corresponding probabilities p and $(1-p)$ respectively, where p is the surface coverage of the metal grains. Under the constraints mentioned above, the problem of obtaining the local field is reduced to the solution of a linear system of Kirchhoff's equations. Written in a matrix form this is given by the equation $H\phi=F$, where the Kirchhoff Hamiltonian $(HK)H$ is a symmetrical matrix with diagonal and off-diagonal elements and the current F depends on the incident field. To find the site potentials $\{\phi_i\}$ we apply the block-elimination procedure,[10] where we impose periodic boundary conditions on the lattice sites. The block-elimination procedure operates with vectors $\phi_j=\{\phi_{j1},\phi_{j2},\ldots,\phi_{jL}\}$ representing potentials in the jth row of the square lattice. Being written in terms of ϕ_j, the Kirchhoff Hamiltonian assumes the form of the tridiagonal block matrix, where each block is an $L\times L$ matrix. The blocks, which are on the diagonal, represent connections inside a row of the square lattice, which we use to describe the film, and therefore have a tridiagonal form. The off-diagonal blocks in the Kirchhoff Hamiltonian represent connections between neighboring rows and have a diagonal form. Using this block structure of the matrix H, we solve the Kirchhoff equations in L^4 elementary operations (L is the lattice size), which is considerably smaller when compared with the L^6 operations needed if Gauss elimination is used.

The local-field distributions for silver-glass composite films at wavelengths of 543 and 633 nm, coinciding with the wavelengths used in our experimental studies, were computed numerically by using the method described above. The images were then averaged over an area corresponding to the resolution limit of the experimental data (120×120 nm^2). This resolution limit was arrived at by accounting for the effective NSOM probe tip-diameter (~50 nm) and the corresponding acceptance angle of the fiber at a tip-sample separation of 10 nm. The electric field vectors at the sample surface have both positive and negative values. The averaging process leads to significant destructive interference, and as a result, the average light intensity is substantially reduced after the averaging process.

The numerical-simulation process for creating silver-glass structures involves random incidence of silver particles onto a glass substrate. A straightforward probability relation can be used to determine metal filling fraction p as a function of deposition time t. Assuming that the metal particles fall individually onto the substrate and surface diffusion is negligible, one can write a simple exponential relation between metal filling fraction p and deposition time t,

$$p=1-\exp(-t/\tau), \tag{2}$$

where parameter $\tau=\beta/SR$. Here S is the area covered by an individual metal particle, R is the deposition rate, i.e., the number of particles added to a unit area of the film per unit time, and β is a numerical factor that depends on the shape of the metal particles. For a circular metal particle, $\beta=1$. A film reaches the percolation threshold at a deposition time $t=t_c$, when the metal filling fraction p is equal to the value at the percolation threshold p_c. We found (see below) that the value $p_c \cong 0.65$ best fits our experimental data. The percolation threshold is not unique, but in general depends on the deposition process.

The effective electric resistance of a metal-dielectric film, ρ, decreases as metal filling fraction or deposition time increases. The largest changes occur in the vicinity of the percolation threshold p_c, i.e., $|p-p_c| \ll \Delta p$, where the effective electric resistance ρ, obeys the power laws

$$\rho \approx \begin{cases} \rho_d(p-p_c)^s & \text{for } \Delta p < p_c - p \ll 1, \\ \rho_m(p_c-p)^{-r} & \text{for } \Delta p < p - p_c \ll 1, \end{cases} \tag{3}$$

where the critical exponents are set as $r=s=1.3$. Assuming that one can treat the film as two dimensional, ρ_m is metal resistance whereas ρ_d is called the tunneling resistance, which is associated with the tunneling of electrons between metal components across the dielectric area of the film.

In the vicinity of the percolation threshold there is a metal coverage range $\Delta p \cong (\rho_m/\rho_d)^{1/(s+r)}$, where the Ohmic and tunneling resistance should be considered on equal terms.[9] The mechanisms of tunneling, resulting in resistance ρ_d, could include (i) tunneling of electrons through defects such as impurities in the dielectric area and (ii) direct quantum tunneling of electrons between the metal components, without any help from defects.[30] The tunneling resistance ρ_d is obviously much greater than the metal resistance ρ_m. In fact, they are related by an exponential expression $\rho_d \sim \rho_m \exp(a/\lambda_t)$ for tunneling through distance a, which can

be either the average distance between two neighboring impurities, for mechanism (i), or the average width of the dielectric gap for the direct tunneling mechanism (ii). The characteristic tunneling length λ_t is given approximately by $\lambda_t \sim \hbar/\sqrt{2mE_F}$, where E_F is the Fermi energy of the metal and m is electron mass.

It can be inferred that the tunneling resistance ρ_d is not a constant, but varies with metal filling fraction p. Electron tunneling through metal clusters is a much more effective process for conducting electricity than the repeated tunneling of electrons through isolated metal particles. Below (but near) the percolation threshold, there exist a large number of metal clusters and their sizes increase quickly with increasing p. As a result, ρ_d decreases with increasing p.[30] This dependence of ρ_d on p is ignored for simplicity in our fitting of experimental data with Eq. (3) (see Fig. 7 and discussion thereof).

IV. RESULTS AND DISCUSSION

A. Morphology and electrical resistance

A series of TEM micrographs of silver-Formvar films with different laser-ablation time durations of 5, 10, 20, 30, 40, and 60 min is shown in Fig. 2. The six images, each 1000×1000 nm^2 in size, were recorded and presented at the same magnification. The dark features in these images represent silver. The filling fraction (surface coverage) p, defined as the percentage of area covered by the silver grains, is calculated from each image. The method is explained further on in the text, and the results are summarized in Table I in the row entitled "Filling fraction p (from TEM images)." The transition from individual metal grains to isolated metal clusters and then to interconnected clusters with an increase in laser-ablation time and the filling fraction can be seen clearly in Fig. 2. Individually separated metal grains are seen in Fig. 2(a) with an average grain size of ~7 nm. The average grain size increases to ~15 nm in Fig. 2(b). The fact that the filling fraction values (from Table I) corresponding to Figs. 2(a) and 2(b) are very close (0.30 and 0.36, respectively) even though the deposition time is doubled indicates that there are some coalescence effects and three-dimensional growth effects due to substrate-metal interaction. For the sample corresponding to Fig. 2(c) the filling fraction increases to about $p=0.45$ and the initiation of cluster formation is evident with individual grain sizes of ~25 nm. With further increase in p, Fig. 2(d) shows an increase in grain sizes and more interconnected clusters of silver at a value of $p=0.62$. Figure 2(e), at a filling fraction of 0.74, again shows further increase in grain size and cluster interconnectivity, and the sample is clearly beyond the percolation threshold. Figure 2(f) is mostly metal with small dielectric voids and, at a value of $p=0.8$, is beyond the percolation threshold. Previous studies of the growth of silver and gold films on glass and rocksalt substrates by thermal evaporation clearly show a dependence of the film morphologies on deposition parameters, and it is reported that for semicontinuous films, an oblique angle of the incident particles causes the formation of a smaller number of large-sized islands (agglomeration).[31] AFM data in the present experiment indicate that the maximum z values perpendicular to the substrate plane during AFM scanning vary from about 10 to 100 nm form deposition times of 5–60 min.

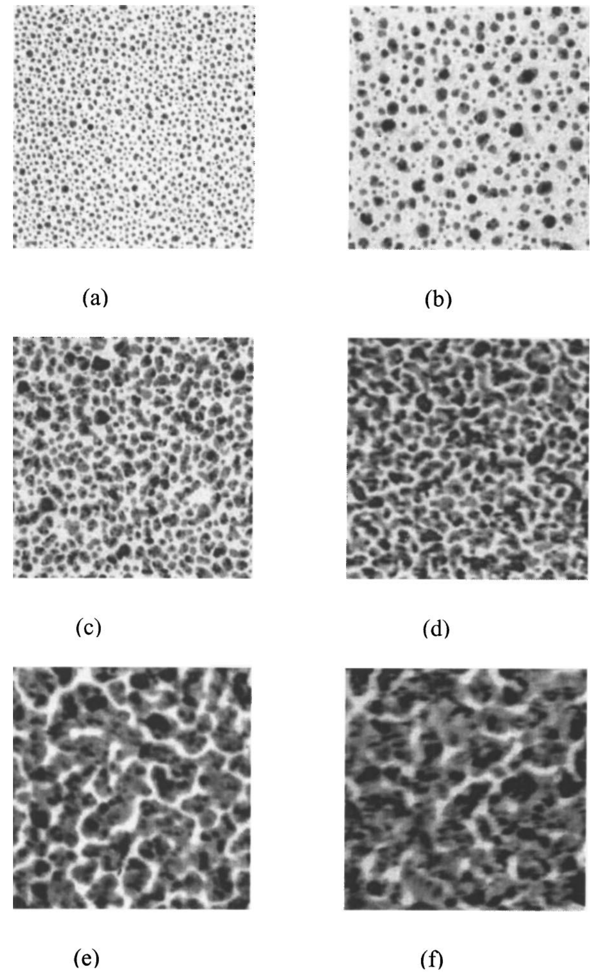

FIG. 2. Transmission electron microscopy images (1×1 μm^2) of silver films at various metal concentrations p corresponding to different deposition times t show a transition from individual metal grains to interconnected clusters. (a) $t=5$ min, (b) $t=10$ min, (c) $t=20$ min, (d) $t=30$ min, (e) $t=40$ min, and (f) $t=60$ min. Filling fractions are given in Table I.

Figure 3 depicts SEM micrographs showing the morphology of the silver films with the purpose of comparing SEM images of silver films on SiO_2 and Formvar substrates. The figure shows a series of 400×400 nm^2 images of silver film deposited on both substrates at a deposition time of 60 min. Figure 3(a) is a SEM image on a SiO_2 surface: Fig. 3(b) is a SEM image on a Formvar substrate. Figures 3(a) and 3(b) show a very close correspondence in terms of particle size, filling fraction (see Table I), and surface morphology, which is evidence of the fact that the difference in substrate chemistry has a limited effect on the film morphology in our case. The filling fraction values at this deposition time are also comparable, as indicated in Table I.

The uncertainty in SEM measurements due to errors in edge identification and other factors has been reported to be several nanometers[32,33] for images of calibration sources with metallic features having sizes of the order of 500 nm.

TABLE I. Metal filling fraction and electrical resistance of the films deposited at different deposition times.

Deposition time t (min)	5	10	20	30	40	60
Filling fraction p (from TEM images)	0.30	0.36	0.45	0.65	0.74	0.83
Filling fraction p (from SEM images)	0.50			0.63		0.85
Electrical resistance (Ω)	6.0×10^{13}	6.0×10^{12}	1.5×10^{13}	5.0×10^{10}	3.0×10^{8}	1.0×10^{8}

Since the average sizes of our silver grains are of the order of 20 nm, the uncertainty in this case is expected to be somewhat less, perhaps ~1 nm. This uncertainty should account for some of the differences between the TEM and SEM images obtained in our studies.

Figure 4 shows TEM and SEM images ($1\times1\ \mu m^2$) at a deposition time of 30 min, before and after image processing. On the left side are the raw gray scale TEM [Fig. 4(a), on a Formvar substrate] and SEM [Fig. 4(c), on a SiO_2 substrate] images before converting to the respective binary black-and-white images obtained after some image processing, shown, respectively, in Figs. 4(b) and 4(d). The raw TEM images in gray scale were processed, and a threshold value for brightness was selected. Above this threshold, a pixel would record as a bright spot (with a value of 1) and, below it, as a dark spot (with a value of 0). The general morphology of the films is preserved in the binary images, although some minor distortions are assumed. The black-and-white images corresponding to each TEM micrograph were then used to compute the filling fraction. The numbers of 1's and 0's were counted to measure the area covered by silver and the area left bare, respectively.

Figure 5 shows theoretically simulated images of the morphology of silver particles on a dielectric substrate at filling fractions of 0.3, 0.5, and 0.7, respectively. The images are $1\times1\ \mu m^2$ in size. As in the experimental TEM and SEM images in Fig. 3, silver is indicated by dark features in Fig. 5. The average grain size in all three images is ~20 nm. This experimentally determined average grain size was chosen as the uniform grain size for numerical simulations. Figure 5(a), at a filling fraction of 0.3, is below the percolation threshold and shows individually separated grains as well as some clusters at the initial stages of their formation. Figure 5(b), at a filling fraction of 0.5, is near the percolation threshold and shows the existence of large interconnected clusters with very few individual grains. Figure 5(c), at a filling factor of 0.7, is well above the percolation threshold and shows the existence of dielectric voids in a primarily metallic film. Figures 2 and 5 indicate a fairly good correspondence between experimentally synthesized samples and theoretically simulated images. The variation in metal particle size in the actual experiment was found to follow a wide log-normal distribution.[34] The effect of this on the local-field intensities and other phenomena is expected to be limited.

Figure 6 is a graph showing the dependence of filling fraction on deposition time. The experimental data are represented by circles. The fact that some amount of image processing is required while calculating the filling fractions in order to obtain a contrast large enough to distinguish between dark and bright pixels in the images contributes to the

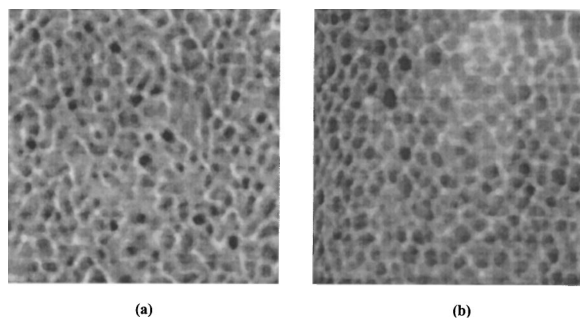

FIG. 3. SEM images ($400\times400\ nm^2$) of silver films on (a) SiO_2 and (b) Formvar substrates at a deposition time of 60 min.

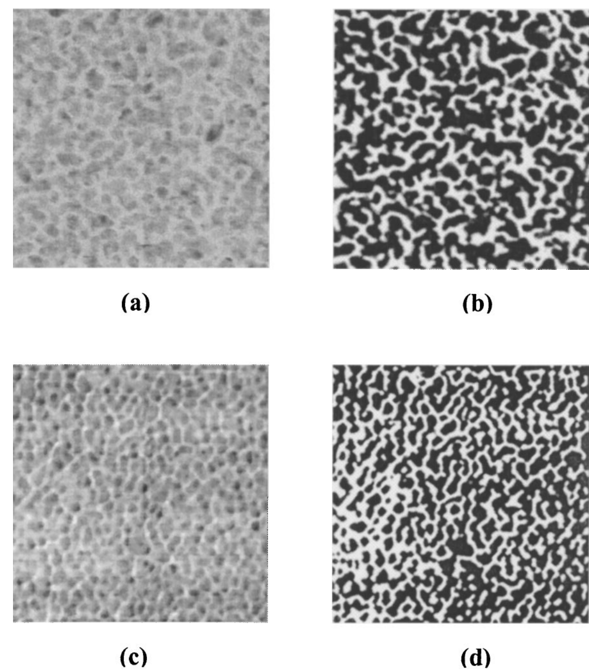

FIG. 4. TEM and SEM images ($1\times1\ \mu m^2$) of silver films before and after image processing at a deposition time of 20 min. TEM image on Formvar substrate (a) before processing and (b) after processing. SEM image on SiO_2 substrate (c) before processing and (d) after processing.

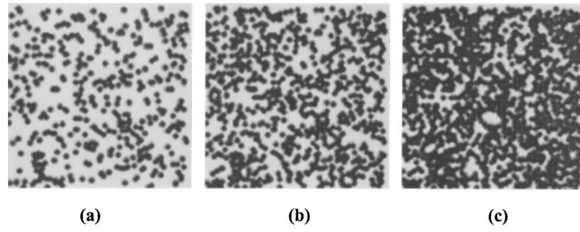

FIG. 5. Theoretically simulated images ($1\times1\ \mu m^2$) of silver films at various metal concentrations p. (a) $p=0.3$, (b) $p=0.5$, and (c) $p=0.7$.

error bars in the experimental data. The difference in substrate properties between glass (for optical and electrical measurements) and Formvar (for the TEM measurements) also contributes to the uncertainty in experimental filling fraction estimates. The contribution to the uncertainty in filling fraction from different substrates is a few percent for films with a deposition time of 10 min or longer (see Table I). The data for the films with a deposition time of 5 min, which exhibit a large difference in the filling fraction between TEM and SEM images, are not used in Fig. 6. This large difference is possibly due to increased effects of the differences in SiO_2 and Formvar substrate energies at low metal concentrations. For deposition times greater than 5 min, the metal concentration is probably large enough so that the silver-silver interaction becomes significant as compared to the silver-substrate interaction. The filling fraction values from SEM and TEM for these deposition times (>5 min) agree well, and optical studies are restricted to such samples. The three numerically calculated curves are obtained from Eq. (2) at three different values of the parameter τ. Within the error margins, the experimental data match best with the numerical curve with τ set at a deposition time of 30 min. The curves with τ set at 25 and 35 min are further from the experimental data. However, all three numerically obtained curves follow the same trend and agree reasonably well with the experiment.

Figure 7 which exhibits the resistance versus filling fraction data, shows that the experimental data (solid circles) dip

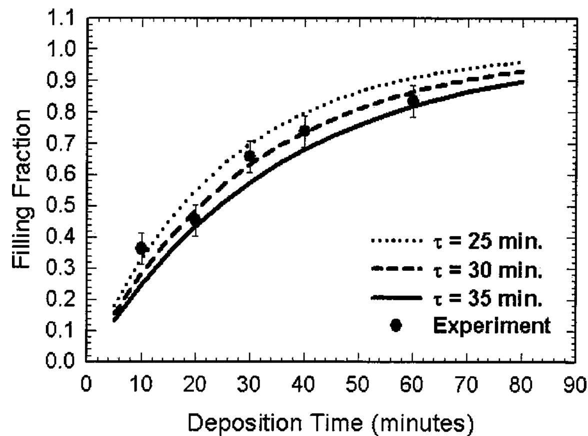

FIG. 6. Filling fraction p vs deposition time t. The theoretical curves are calculated using Eq. (2) with p_c set at three different deposition times of 25, 30, and 35 min.

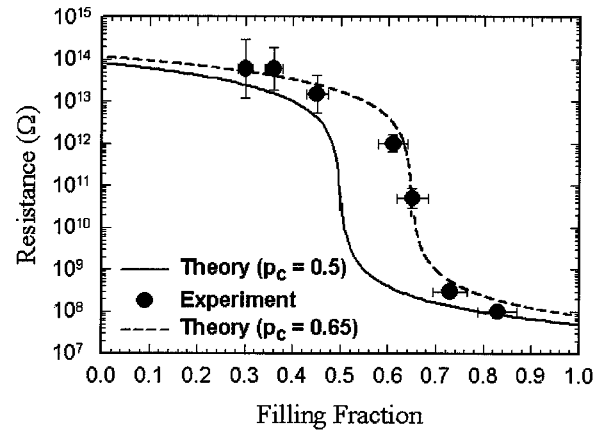

FIG. 7. Electrical resistance vs filling fraction. The theoretical curves are plotted in accordance with Eq. (3).

sharply between filling fraction values of 0.45 and 0.75 with the midpoint of the drop being at about $p=0.65$, which corresponds to a deposition time of 30 min. The resistance drops from approximately 10^{13} to 10^8 Ω between filling fraction values of 0.45 and 0.75. The numerically calculated curves in the figure were obtained from the parametric equation (3) with the fitting parameters $\rho_d=10^{14}$ Ω (the experimentally measured value for pure glass film) and $\rho_m=10^7$ Ω (the experimentally measured value for a mostly metal film) and setting $p_c=0.5$ (solid line) and $p_c=0.65$ (dashed line). The dashed line follows our experimental data most closely and thus sets the percolation threshold at $p_c=0.65$, which is somewhat larger than the theoretically predicted value of $p_c=0.5$–0.6.[2,9,34] Similar studies of resistance with coverage on samples of indium oxide deposited on glass by reactive evaporation show an increase in conductance of about the same order of magnitude as the present study.[35] Studies of deposition via laser ablation of semicontinuous copper films on Pyrex substrates[36] show larger drops in electrical resistance compared to the present data. There have also been studies of gold films of thickness values between 5 and 35 nm on mica substrates which also display a sharp drop in resistance.[37] However, the present data do mark the percolation threshold at a value consistent with filling fraction estimates of 0.65 as found in this study and others.[38] Some of the differences between theoretical and experimental data in this study can be attributed to uncertainties in the filling fraction calculations and errors in the resistance measurements. Three-dimensional growth effects in the silver film, which are not considered in our theoretical model of the metal-dielectric film, are very likely an important factor in these differences.

It is expected that surface diffusion, which results in the migration of particles between grains and promotes the formation of larger islands at the cost of smaller ones,[39] also helps in the formation of elevated islands instead of purely two-dimensional ones. This would mean that for the same deposition time, the actual contact area of metal with glass in such films would be less than that obtained from the model for silver deposition described in the theoretical discussion. Surface diffusion in thin films and its effect on island forma-

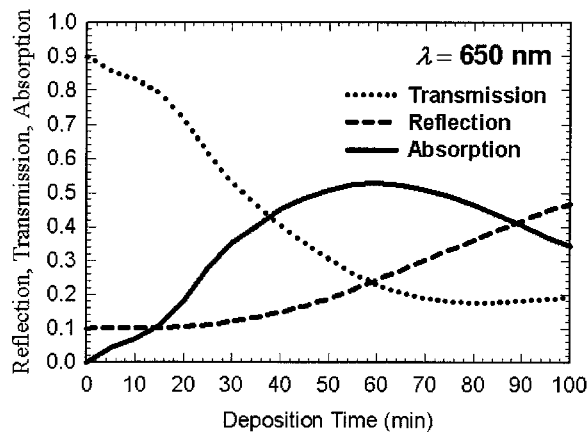

FIG. 8. Transmission, reflection, and absorption vs deposition time at a wavelength of 650 nm. The *in situ* data reveal an absorption peak.

tion and growth is a well investigated topic and has been studied experimentally and modeled numerically as well.[39–42] The nucleation growth kinetics such as island formation and coalescence, etc., in thin films has been studied in detail in the past.[43] The diffusion coefficient is dependent on the adatom coverage of the substrate, and at low coverage, adatom-substrate interactions play a strong role, whereas at higher coverage adatom-adatom interactions must be considered as well.[42] Studies of gold deposited on crystalline and amorphous polymer substrates show that the adatom surface diffusion coefficients have the same order of magnitude for both crystalline and amorphous substrate phases at room temperature.[40] Also, the diffusion coefficients for gold on high-density polyethylene substrates have very close values both above the glass transition temperature and below it, with a steep slope near the transition.[40] Therefore, in our experiments with amorphous substrates, the diffusion coefficient may be considered comparable to that obtained from studies on crystalline substrates. In that connection, it was shown in more recent experimental studies of silver deposited on copper substrates that surface diffusion effects play a strong role at temperatures above 285 K.[41] It is therefore safe to assume that surface diffusion has a tangible effect in our samples, which are analyzed at temperatures above 275 K. From TEM and SEM studies, it is clear that the films are not purely two dimensional in that elevated islands are formed in the silver-glass films, but the formation of a well-developed three-dimensional network of metallic conducting channels is still not completed. Therefore, it is believed this situation does not pertain to three-dimensional percolation theory since the effective electrical elements (conducting silver channels or insulating dielectric channels) in the silver-glass composites are still on the two-dimensional plane where the silver and glass are in contact. It is inferred that the formation of elevated islands and consequent decrease in silver-glass contact area results in a percolation threshold corresponding to a higher metal concentration as compared to bond percolation estimates.

Figure 8 is a plot of reflection and transmission data with a diode laser operating at 650 nm as the incident beam and obtained *in situ* during laser ablation. The absorption coefficient was calculated numerically as the difference between the transmission and reflection data. The transmission coefficient shows a relatively sharper drop after a deposition time of 25 min, dropping to 50% of its original value at 30 min. There is also an indication of a slight increase in transmission at deposition times greater than 90 min. The reflection coefficient, which holds steady up to a deposition time of 20 min, then shows a steady increase with deposition time. The plot shows a strong absorption peak with a maximum value greater than 50%—the value previously measured at the percolation threshold by others.[2,27] In our samples the percolation threshold is expected to correspond to a deposition time of 30 min. However, at this value, the absorption coefficient, which is ~40% at p_c, then slowly rises to its peak value of ~55% at a deposition time of 55 min. This may be due to the fact that scattering losses, which would be particularly strong as the film gets thicker and has a more irregular surface, are neither included in the theoretical model nor corrected for in our experiments. Absorption peaks in silver and gold have been experimentally observed in the past,[43] and the peak wavelength is known to be an increasing function of film thickness up to values of 10 nm for silver.[44] The high absorption predicted in previous theoretical and experimental work is verified by these data.

B. Near-field optical properties at the percolation threshold

The following is a discussion of the local optical properties of the silver-glass film at the percolation threshold.

Near-field intensity profiles experimentally recorded over a 4×4 μm^2 area for a sample near the percolation threshold ($t=30$ min and $p=0.65$) are shown, respectively, in Figs. 9(a), 9(b), and 9(c) at an illumination wavelength of 543 nm and in Figs. 9(d), 9(e), and 9(f) at an illumination wavelength of 633 nm. The images exhibit a very nonuniform distribution of near-field optical intensity. The role of localized surface plasmons in such nonuniform intensity distributions is a well-studied phenomenon and explained in detail in previous work.[1,3,4,7,25]

Figure 9(a) shows the experimentally observed near-field intensity profile with peak intensities reaching values as high as 20 times the intensity of the incident evanescent wave. Figures 9(b) and 9(c) show theoretically calculated near-field optical intensity profiles of a film at the percolation threshold with filling fraction $p=p_c=0.5$, with and without averaging, respectively. The value of $p=0.5$ was chosen since it corresponds with the exact value of the percolation threshold for the bond percolation lattice that is used in the theoretical model. The averaging process was carried out in order to effectively compare theory with experiment, the latter being limited by the resolution of the NSOM (120 nm). The resulting averaged theoretical distribution is shown in Fig. 9(b). The experimental data [Fig. 9(a)] and the theoretically computed result after the averaging process [Fig. 9(b)] closely resemble each other. They have similar general features and consistent peak enhancement factors of 20–30. It should be emphasized, however, that the exact distributions of the near-field optical intensity, such as the exact peak positions and exact peak heights, in these two images should not be com-

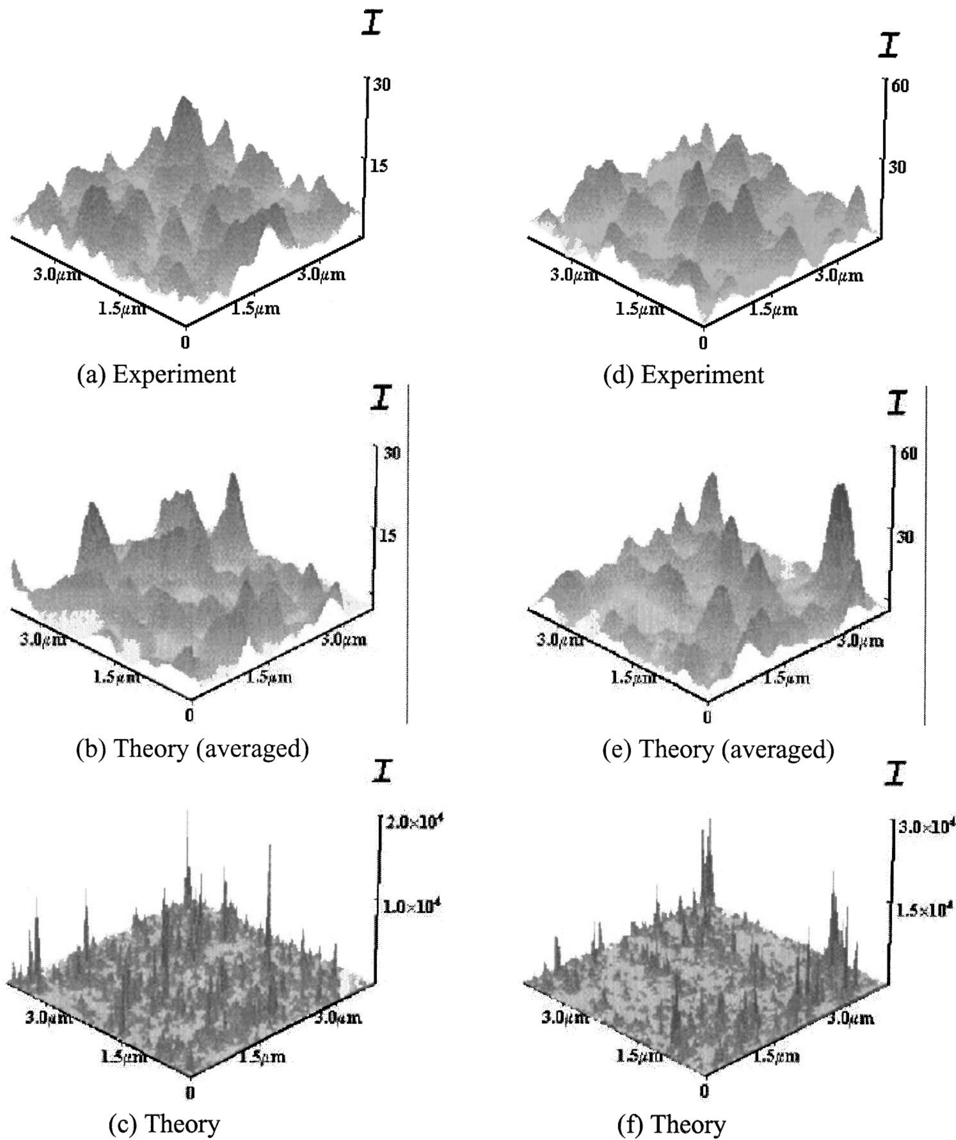

FIG. 9. Experimental, averaged theoretical, and raw theoretical optical intensity images over a $4\times4\ \mu\mathrm{m}^2$ area at $p\approx p_c$. Images in the column on the left [(a), (b), and (c)] are at an illumination wavelength of $\lambda=543$ nm, and those in the column on the right [(d), (e), and (f)] are at an illumination wavelength of $\lambda=633$ nm. The first row [(a) and (d)] displays experimental NSOM data. The second row [(b) and (e)] shows theoretical data after the averaging process. The third row [(c) and (f)] show raw theoretical data.

pared because the films used for the experimental studies and theoretical calculations have different arrangements of the metal clusters.

Figure 9(c), which shows the theoretical local-field intensity over a $4\times4\ \mu\mathrm{m}^2$ area, has optical feature sizes that are comparable to the particle sizes in the sample (~20 nm). The image is comprised of a large number of highly intense localized peaks (hot spots) spread over the sample. The values for the maximum enhancement factors in these peaks are extremely high (up to $\sim10^4$). Although not evident in Figs. 9(a) and 9(b), where the absolute value squared of the local fields is shown (the applied field is assumed to have a magnitude of 1), it is important to note that the local-field vectors are distributed uniformly about zero with comparable numbers of positive and negative values. On comparing Figs. 9(a) and 9(b) with Fig. 9(c), it is evident that there is a significant drop in the field intensities in the former, an effect that is due to destructive interference and the mutual cancellation of the field vectors during the averaging process. There is, however, a degree of preservation of large-scale local-field topology in Fig. 9(b) in that the majority of high-intensity local field features (groups of peaks which are in spatial proximity) seen in Fig. 9(c) are generally preserved in Fig. 9(b) as well.

In Fig. 9(d) the experimentally obtained near-field intensity profile over the same $4\times4\ \mu\mathrm{m}^2$ area of the sample used for Fig. 9(a) ($t=30$ min and $p=0.65$) at an illumination wavelength of 633 nm is shown. The corresponding theoretical calculations, with and without averaging, respectively, are shown in Figs. 9(e) and 9(f). The averaging process results in the same effects of an increase in feature sizes and a decrease in peak intensities as described for Figs. 9(a), 9(b), and 9(c). Again, the images exhibit a very nonuniform distribution of near-field optical intensity with peak intensities reaching values as high as 40 times the incident intensities for Figs. 9(d) and 9(e) and 10^4 times the incident intensity for Fig. 9(f).

It should be noted that the average enhancement factors increase with wavelength in our studies, as is evident on comparing images from the two wavelengths in Fig. 9. This wavelength dependence of the average local-field enhancement has been predicted by scaling theory.[6,8] It should also

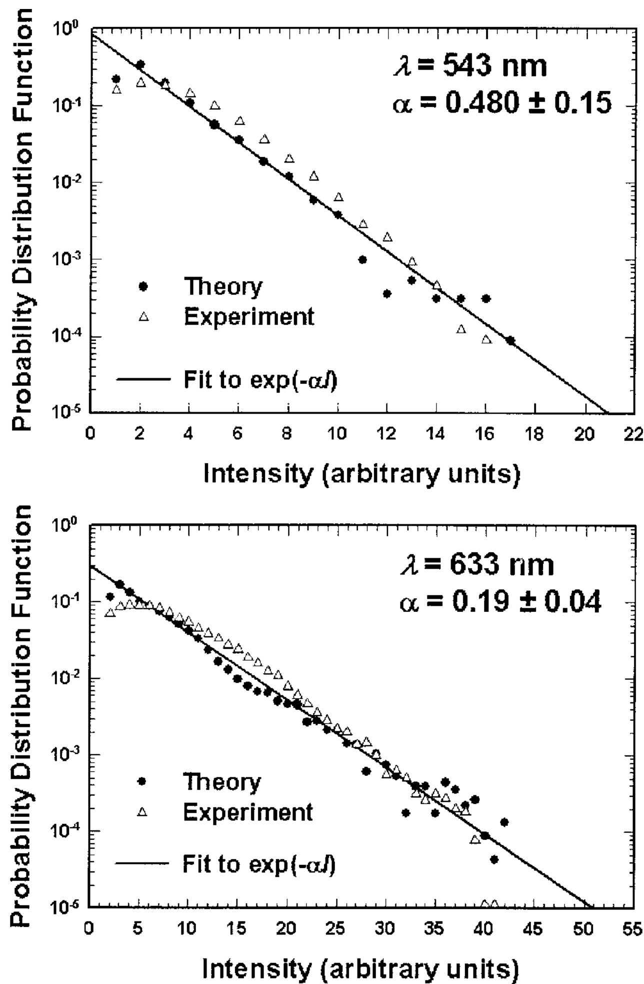

FIG. 10. Probability distribution functions of experimental and averaged theoretical data at $p \cong p_c$ at an illumination wavelength of (a) $\lambda = 543$ nm and (b) $\lambda = 633$ nm.

be noted that the exact locations of peaks depend on the wavelength of illumination.

The differences between the images at illumination wavelengths of 543 and 633 nm can be understood more clearly from the probability distribution functions shown in Fig. 10. These data are calculated from experimental NSOM data and corresponding averaged theoretical data at wavelengths $\lambda = 543$ and 633 nm. The data were fitted to an exponential function $\exp(-\alpha I)$. The PDF's from raw theoretical data follow a wide log-normal distribution.[10] However, during the averaging process, there are changes in both the magnitude of the near-field enhancement factors and the shape of the probability distribution. As a result, the PDF transforms from a log-normal to an exponential distribution. The experimental and theoretical PDF's shown in Figs. 10(a) and 10(b) are in close agreement, and the calculated linear regression lines have very small error bars. It is important to note that the tail of the distribution for $\lambda = 633$ nm shows an enhancement factor of 50, which is twice as large as that for $\lambda = 543$ nm. The average enhancement factors thus increase with wavelength as predicted by scaling theory.

C. Below and above the percolation threshold

In Figs. 11(a), 11(b), and 11(c) the experimental, averaged theoretical, and raw theoretical images, respectively, over a 4×4 μm^2 area at a metal concentration ($p = 0.37$) less than the percolation threshold are shown. Figures 11(d), 11(e), and 11(f) are the corresponding images above the threshold at $p = 0.74$. The averaged theoretical images have again been calculated by the method described earlier and show the same qualitative agreement with the experimental NSOM images. Again, the NSOM images show a highly nonuniform distribution of local optical intensity with peak intensities reaching values as high as 30 times the intensity of the incident wave. However, on comparing Fig. 9(d) with Figs. 11(a) and 11(d) (all recorded at a wavelength of 633 nm) it is evident that the density of intensity peaks is smaller in the latter cases. Thus, at both $p < p_c$ and $p > p_c$, the distance between the intensity peaks is larger in comparison with the distances at $p = p_c$, which indicates stronger localization at both $p < p_c$ and $p > p_c$. This is also seen on comparing the corresponding averaged theoretical [Figs. 9(e) with Figs. 11(b) and 11(e)] and raw theoretical images [Fig. 9(f) with Figs. 11(c) and 11(f)]. In all these cases, the enhancement factors of individual peaks are higher than that observed at $p = p_c$, but the surface density of peaks is lower in comparison. We can conclude that these properties of the field distribution are preserved at larger scales as well.

D. Optical response at high metal concentrations

Figure 12 pertains to the experimentally obtained local optical properties of certain special features in samples with high metal concentrations ($p > 0.80$).

Figures 12(a) and 12(d) exhibit surface morphologies (AFM scans) obtained from the NSOM probe and recorded over two 10×10 μm^2 areas, respectively, for a sample with a high metal concentration ($t = 60$ min and $p = 0.85$). It should be noted that due to the relatively large tip-radius of the NSOM probe (50 nm) as compared to conventional AFM probes, the resolution for the surface morphology is inferior in comparison, but sufficient to display the features under consideration in this section. Both images exhibit a fairly uniform background, similar to what is shown in Fig. 2(f), plus an elevated structure near the center of the images. On examining scan lines in detail, it is evident that each of these structures has the form of a crater, with a hole surrounded by a ring of material, the ring being higher than the surrounding basal plane and the hole being lower than it. The elongation of the features in the diagonal direction is attributed to the vibration amplitude of the oscillating probe tip. While examining AFM scan lines, the diameters of the central hole were obtained by taking the full width at half maximum of the dip in the scan line. This value was averaged over several consecutive scan lines. The corresponding hole diameter for Fig. 12(a) was found to be about 0.25 μm, and for Fig. 12(d), the hole size is about 0.4 μm. This kind of structure was also observed in electron microscopy studies. Figure 13 shows a 1.5×1.5 μm^2 TEM micrograph of such an area in a sample under identical deposition conditions. The size of the hole in this image is about 0.25 μm. Such holes are formed during

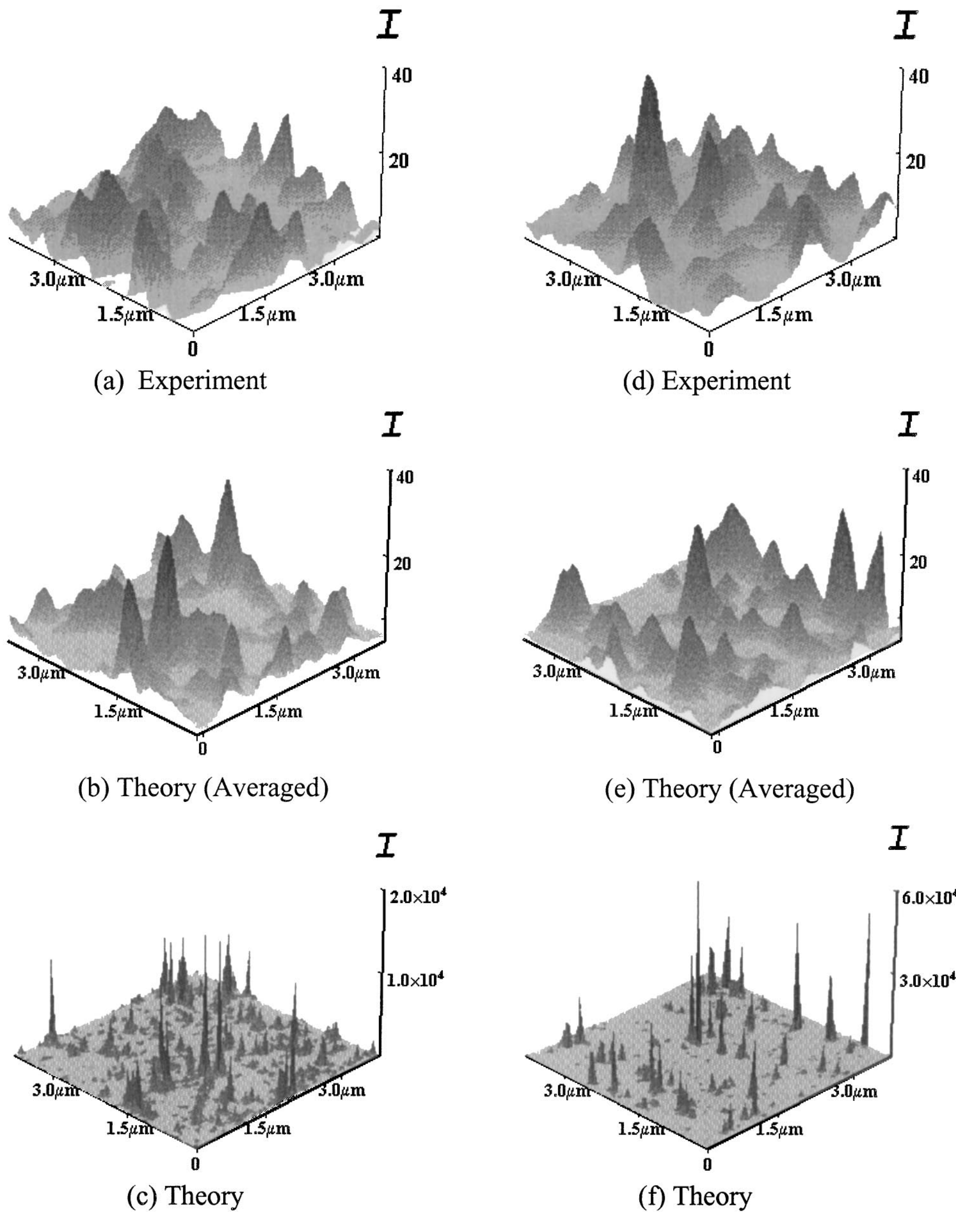

FIG. 11. Experimental, averaged theoretical, and raw theoretical optical intensity images over a $4\times4\ \mu\mathrm{m}^2$ area at $\lambda=633$ nm for $p<p_c$ and $p>p_c$. Images in the column on the left [(a), (b), and (c)] are at a metal concentration $p<p_c$, and those in the column on the right [(d), (e), and (f)] are at a metal concentration $p>p_c$. The first row [(a) and (d)] displays experimental NSOM data. The second row [(b) and (e)] shows theoretical data after an averaging process. The third row [(c) and (f)] shows raw theoretical data.

sample synthesis by laser ablation when submicrometer-sized droplets are occasionally ejected from the target surface and deposited on the glass substrate. If the droplet is formed at an early stage of the entire deposition period, holes are formed in the leeward (shadow region) of the droplet, which forms a blockade for additional incoming silver atoms ejected from the target. The TEM image shows the small droplet and the larger shadow region devoid of silver that is formed adjacent to it. Outside the hole, the sample surface is almost all silver with very narrow paths devoid of silver across the surface. It was found from AFM and TEM images that, on an average, one submicron void was formed over every $20\times20\ \mu\mathrm{m}^2$ scan area in the sample.

The rest of the four images in Fig. 12 are the $10\times10\ \mu\mathrm{m}^2$ NSOM images corresponding to the surface morphology scans shown in Figs. 12(a) and 12(d), respectively. Figures 12(b) and 12(e) in the second row are recorded at 543 nm, and Figs. 12(c) and 12(f) in the third row are recorded at 633 nm. All four images show very bright regions corresponding to the position of the holes observed in the AFM scans. What is most remarkable about the optical images is the very high intensity of the bright spots—more than 100 times brighter than the incident intensity and many times brighter than hot spot intensities observed at lower silver coverage. The optical responses of such features are sensitive to wavelength, as is evident on comparing Fig. 12(b) with 12(c) and Fig. 12(e) with 12(f). In our samples, it is evident from Fig. 13 that the area surrounding the dielectric void is mostly metal, but not fully so, and there are narrow dielectric channels running through the metal matrix. Therefore, the optical intensity distribution consists of a background of enhancement peaks of lesser magnitude, which are dwarfed by the high-intensity peaks near the void.

The concentration of the electromagnetic fields near a hole reported here resembles the field concentration in an array of subwavelength holes. Extraordinary optical trans-

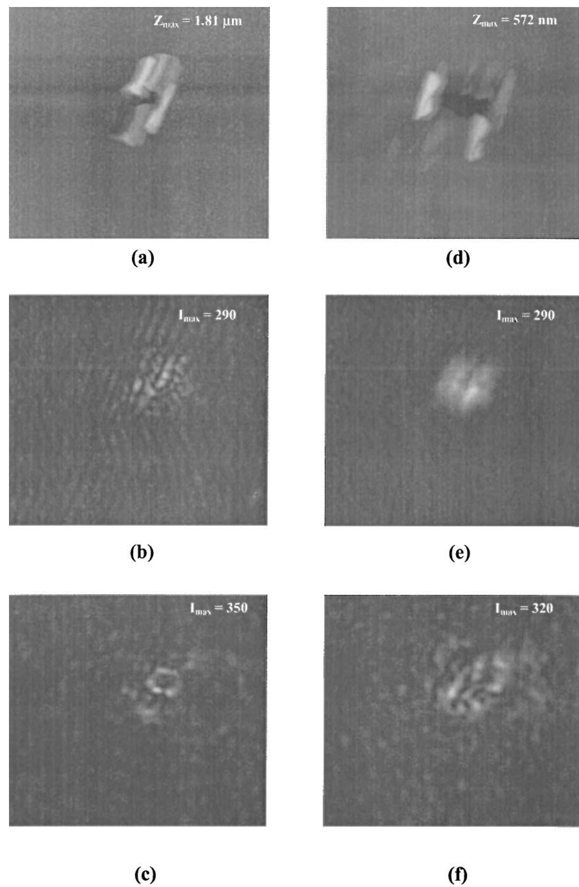

FIG. 12. Experimental AFM and corresponding NSOM images of a silver film at high metal concentration (deposition time $=60$ min) over a $10\times10\ \mu\text{m}^2$ area at $\lambda=633$ and 543 nm. The relevant feature is the void in the metal film. Images in the column on the left [(a), (b), and (c)] are from one sample area, and those in the column on the right [(d), (e), and (f)] are from another sample area. The first row [(a) and (d)] displays AFM data. The second row [(b) and (e)] shows NSOM images at a probe wavelength of $\lambda=543$ nm. The third row [(c) and (f)] shows NSOM images at a probe wavelength of $\lambda=633$ nm.

mittance through metal films with regular arrays of subwavelength holes has been discovered in the seminal work of Refs. 32 and 45 and has been intensively investigated.[46–51] Apart from fundamental interest this new optical phenomenon could have important applications in subwavelength lithography, wavelength-tunable filters, optical modulators, and flat-panel displays, among other possibilities.[39]

The most common explanation of extraordinary optical transmittance is based on the assumption that the incident light excites surface plasmon-polaritons (SPP's) in the metal film when its wavelength coincides with one of the spatial periods of the array of holes. This results in a resonant interaction of the SPP with the regular array of subwavelength holes and causes a huge enhancement of the light transmittance though the film. Thus the periodicity of the holes plays a crucial role in the theory.[52] In contrast to these speculations our experimental results show that the local electromagnetic field could be strongly enhanced even in a single void in the metal film. We speculate that in this case we observe local-

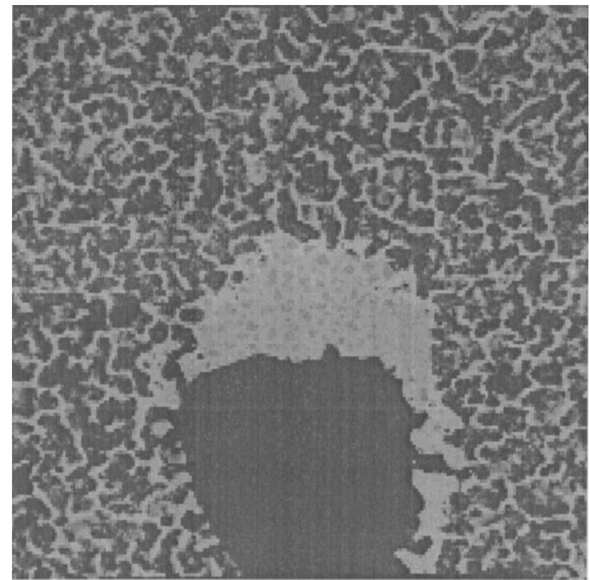

FIG. 13. TEM image ($1.5\times1.5\ \mu\text{m}^2$) of dielectric region surrounded by metal film of high filling fraction.

ization of SPP's in the vicinity of near-wavelength-sized voids. The electric field of the localized SPP has a rather complicated structure with maxima distributed over the area of the film that are larger than the geometric size of the defect in the metal film. The structure of the SPP depends on the wavelength λ and changes significantly with even moderate increases in wavelength—from $\lambda=543$ to 633 nm. The possibility of SPP localization in subwavelength apertures is discussed in recent work[53] where it is suggested that localized SPP could enhance the transmittance through the metal film even when holes are distributed randomly over the film. Another important result of SPP localization is the potential of using these SPP's for nanoscale light circuiting through a linear array of the aforementioned voids.

Such huge enhancement of the local fields in submicron voids in a percolating metal film has been observed for the first time and is in agreement with our transmittance data as well. Indeed, the transmittance does not vanish even for metal concentrations far above the percolation threshold where the film should operate as a perfect mirror. Instead, the transmittance saturates at a value of about 20% and even indicates a tendency to *increase* with an increase in film thickness. We attribute this unusual behavior of the bulk transmittance to transmittance through the submicron voids. The field intensity in the voids is more than 100 times the intensity of the impinging wave. These giant fields operate as secondary sources, generating electromagnetic waves which are emitted from the opposite side (with respect to the side on which light is incident) of the film and resulting in extraordinary transmittance. The amplitudes of the resonance fields in the voids can be large for optically thick films and, as shown in Ref. 53, could even increase with the film thickness.

We infer that the percolation nature of our metal films is very important for the observed extraordinary transmittance. Films with metal concentration far above the percolation threshold have local metallic properties, which satisfy the

conditions for the localization of SPP's.[53] Yet the film remains nonuniform on scales larger than the size of a hole and therefore does not support the propagation of the SPP. This results in a decrease in the radiative decay of the localized plasmon polaritons and promotes the localization of the electromagnetic energy near the voids. These speculations are confirmed by the experimentally observed field distribution around a void (see Fig. 12). The enhanced field overflows out of the void, but only within a distance comparable to the void size. The detailed theory of this phenomenon is under investigation

V. CONCLUSIONS

The following conclusions can be drawn from our experimental and theoretical studies of silver films deposited on insulator substrates.

(1) Based on the morphology and electrical resistance measurements, the percolation threshold in the metal-dielectric composites occurred at a deposition time of about 30 min for the deposition conditions used in our experiments and at a metal filling fraction of ~65%. The latter value is higher than the 50%–60% value predicted for two-dimensional (2D) random bond or site films, suggesting the importance of 3D growth and surface diffusion in our system.

(2) A careful TEM and SEM study of silver films grown on SiO_2 and Formvar substrates shows that the films grown at these two types of substrates are very similar at both medium and high metal coverages. Significant differences, however, have been observed at low metal coverages.

(3) The NSOM images obtained show strong enhancement of the local fields through the existence of hot spots with high intensities. For local optical studies, comparison between experimental data and a numerical model based on the block-elimination method has been made. An exponential probability distribution function was obtained from the experimental images and was in good agreement with the theoretically calculated distribution. From both theory and experiment, the optical enhancement observed at the percolation threshold is quite different from that observed at higher and lower metal concentrations, where stronger localization and an increase in individual peak intensities are observed. It was also observed that both the localization and intensities of the hot spots depend on the incident wavelength.

(4) At a very high metal coverage (>80%), very strong local fields, ~10 times higher than that observed at lower coverage, were observed at some locations of the film. This feature is associated with submicron-sized voids in the metal film and results in extraordinary optical transmittance through the percolation metal films.

ACKNOWLEDGMENTS

This project is supported in part by the Army Research Office (Grant No. DAAD19-01-1-0682), NASA (Grant Nos. NAG8-1710 and NCC5-514), National Science Foundation (Grant No. DMR0121814), and New Mexico Universities Collaborative Research Program at Los Alamos National Laboratory. The authors acknowledge technical assistance provided by Dr. S. Ghoshroy, Dr. L. Trillo, M. Barela, and Dr. R. Liefeld and experimental assistance provided by J. Alderete and D. Smirnova.

*Also at Department of Chemical Engineering, New Mexico State University, Las Cruces, New Mexico 88003-8001.

[1] V. M. Shalaev, *Nonlinear Optics of Random Media: Fractal Composites and Metal-Dielectric Films* (Springer, Berlin, 2000).
[2] D. Stauffer and A. Aharony, *Introduction to Percolation Theory*, 2nd ed. (Taylor & Francis, Philadelphia, 1991).
[3] A. K. Sarychev and V. M. Shalaev, in *Optics of Nanostructured Materials*, edited by V. A. Markel and T. F. George (Wiley, New York, 2000).
[4] A. K. Sarychev and V. M. Shalaev, Phys. Rep. **335**, 276 (2000).
[5] V. A. Shubin, A. K. Sarychev, J. P. Clerc, and V. M. Shalaev, Phys. Rev. B **62**, 11 230 (2000).
[6] A. K. Sarychev and V. M. Shalaev, in *Optical Properties of Nanostructured Random Media*, Topics in Applied Physics, Vol. 82, edited by V. M. Shalaev (Springer, Berlin, 2002).
[7] V. M. Shalaev and A. K. Sarychev, Phys. Rev. B **57**, 13 265 (1998).
[8] A. K. Sarychev, V. A. Shubin, and V. M. Shalaev, Phys. Rev. B **60**, 16 389 (1999).
[9] D. J. Bergman and D. Stroud, Solid State Phys. **46**, 147 (1992).
[10] D. A. Genov, A. K. Sarychev, and V. M. Shalaev (unpublished).
[11] S. Gresillon *et al.*, Phys. Rev. Lett. **82**, 4523 (1999).
[12] M. I. Stockman, L. N. Pandey, L. S. Muratov, and T. F. George, Phys. Rev. Lett. **72**, 2486 (1994).
[13] A. K. Sarychev and V. M. Shalaev, Physica A **266**, 115 (1999); A. K. Sarychev, V. A. Shubin, and V. M. Shalaev, Phys. Rev. E **59**, 7239 (1999); F. Brouers, S. Blancher, A. N. Lagarov, A. K. Sarychev, P. Gadenne, and V. M. Shalaev, Phys. Rev. B **55**, 13 234 (1997); P. Gadenne, F. Brouers, V. M. Shalaev, and A. K. Sarychev, J. Opt. Soc. Am. B **15**, 68 (1998).
[14] S. Ducourtieux, S. Gresillon, A. C. Boccara, J. C. Rivoal, X. Quelin, P. Gadenne, V. P. Drachev, W. D. Bragg, V. P. Safonov, V. A. Podolskiy, Z. C. Ying, R. L. Armstrong, and V. M. Shalaev, J. Nonlinear Opt. Phys. Mater. **9**, 105 (2000).
[15] V. M. Shalaev, Phys. Rep. **272**, 61 (1996).
[16] S. Ducourtieux, V. A. Podoskiy, S. Gresillon, S. Buil, B. Berini, P. Gadenne, A. C. Boccara, J. C. Rivoal, W. D. Bragg, K. Banerjee, V. P. Safonov, V. P. Drechev, Z. C. Ying, A. K. Sarychev, and V. M. Shalaev, Phys. Rev. B **64**, 5403 (2001).
[17] S. I. Bozhevolnyi and V. Coello, Phys. Rev. B **64**, 5414 (2001).
[18] W. D. Bragg, V. A. Markel, W. Kim, K. Banerjee, M. R. Young, J. G. Zhu, R. L. Armstrong, Y. E. Danilova, V. P. Safonov, V. M. Shalaev, and Z. C. Ying, J. Opt. Soc. Am. B **18**, 698 (2001).
[19] S. I. Bozhevolnyi, Phys. Rev. B **54**, 8177 (1996).
[20] S. I. Bozhevolnyi, V. A. Markel, V. Coello, W. Kim, and V. M. Shalaev, Phys. Rev. B **58**, 11 441 (1998).
[21] K. Kneipp, Y. Wang, H. Kneipp, L. T. Perelman, I. Itzkan, R. R. Dasari, and M. S. Feld, Phys. Rev. Lett. **78**, 1667 (1997).
[22] *Materials for Optical Limiting*, edited by R. Crane, K. Lewis, M. Khoshnevisan, and E. Van Stryland, Mater. Res. Soc. Symp.

Proc. No. 374 (Materials Research Society, Pittsburgh, 1995); *Materials for Optical Limiting II*, edited by P. Hood, K. Lewis, R. Pachter, J. W. Perry, D. Hagan, and R. Sutherland, Mater. Res. Soc. Symp. Proc. No. 479 (Materials Research Society, Pittsburgh, 1997).

[23] A. I. Plekhanov, G. L. Plotnikov, and V. P. Safonov, Opt. Spectrosc. **71**, 451 (1991).

[24] M. Ohring, *The Materials Science of Thin Films* (Academic, San Diego, 1992)

[25] S. I. Bozhevolnyi, B. Vohnsen, A. V. Zayats, and I. I. Smolyaninov, Surf. Sci. **356**, 268 (1996).

[26] Y. Yagil, P. Gadenne, C. Julien, and G. Deutscher, Phys. Rev. B **46**, 2503 (1992).

[27] A. K. Sarychev, D. J. Bergman, and Y. Yagil, Phys. Rev. B **51**, 5366 (1995).

[28] S. I. Bozhevolnyi, B. Vohnsen, E. A. Bozhevolnaya, and S. Berntsen, J. Opt. Soc. Am. A **13**, 2381 (1996).

[29] M. Lee, E. B. McDaniel, and J. W. P. Hsu, Rev. Sci. Instrum. **67**, 1468 (1996).

[30] A. K. Sarychev and F. Brouers, Phys. Rev. Lett. **73**, 2895 (1994).

[31] K. L. Chopra and M. R. Randlett, J. Appl. Phys. **39**, 1874 (1968).

[32] J. S. Villarrubia, A. E. Vladr, J. R. Lowney, M. T. Postek, R. A. Allen, M. V. Cresswell, and R. N. Ghoshtagore, Proc. SPIE **3998**, 84 (2000).

[33] J. S. Villarrubia, R. Dixson, S. Jones, J. R. Lowney, M. T. Postek, R. A. Allen, and M. W. Cresswell, Proc. SPIE **3677**, 587 (1999).

[34] C. G. Granqvist and O. Hunderi, Phys. Rev. B **16**, 3513 (1977).

[35] V. Korobov, M. Leibovitch, and Yoram Shapira, Appl. Phys. Lett. **65**, 2290 (1994).

[36] S. K. So, H. H. Fong, C. F. Yeung, and N. H. Cheung, Appl. Phys. Lett. **77**, 1099 (2000).

[37] K. L. Chopra, J. Appl. Phys. **37**, 2249 (1966).

[38] C. K. Shek, G. M. Lin, J. K. L. Lai, and J. L. Li, Thin Solid Films **300**, 1 (1997).

[39] B. Fischer, H. Brune, J. V. Barth, A. Fricke, and K. Kern, Phys. Rev. Lett. **82**, 1732 (1999).

[40] F. Katzenberg, R. Janlewing, and J. Petermann, Colloid Polym. Sci. **278**, 280 (1999).

[41] C. Douketis, T. L. Haslett, Z. Wang, M. Moskovits, and S. Iannotta, J. Chem. Phys. **113**, 11315 (2000).

[42] Roger C. Baetzold, in *Metal-Surface Reaction Energetics*, edited by E. Shustorovich (VCH, New York, 1991).

[43] K. L. Chopra, *Thin Film Phenonema* (McGraw-Hill, New York, 1969).

[44] R. Payan and G. Rasigni, J. Phys. Radium **25**, 92 (1964).

[45] T. W. Ebbesen, H. J. Lezec, H. F. Ghaemi, T. Thio, and P. A. Wolff, Nature (London) **391**, 667 (1998).

[46] H. F. Ghaemi, T. Thio, D. E. Grupp, T. W. Ebbesen, and H. J. Lezec, Phys. Rev. B **58**, 6779 (1998).

[47] T. J. Kim, T. Thio, T. W. Ebbesen, D. E. Grupp, and H. J. Lezec, Opt. Lett. **24**, 256 (1999).

[48] T. Thio, H. F. Ghaemi, H. J. Lezec, P. A. Wolff, and T. W. Ebbesen, J. Opt. Soc. Am. B **16**, 1743 (1999).

[49] D. E. Grupp, H. J. Lezec, T. W. Ebbesen, K. M. Pellerin, and T. Thio, Appl. Phys. Lett. **77**, 1569 (2000).

[50] A. Dogariu, T. Thio, L. J. Wang, T. W. Ebbesen, and H. J. Lezec, Opt. Lett. **26**, 450 (2001).

[51] C. Sonnichsen, A. C. Duch, G. Steininger, M. Koch, G. von Plessen, and J. Feldmann, Appl. Phys. Lett. **76**, 140 (2000).

[52] L. Martin-Moreno, F. J. Garcia-Vidal, H. J. Lezec, K. M. Pellerin, T. Thio, J. B. Pendry, and T. W. Ebbesen, Phys. Rev. Lett. **86**, 1114 (2001).

[53] A. K. Sarychev, V. A. Podolskiy, A. M. Dykhne, and V. M. Shalaev, IEEE J. Quantum Electron. **38**, 956 (2002).